

NeptuniumV retention by siderite under anoxic conditions: Precipitation of NpO₂-like nanoparticles and of NpIV pentacarbonate

Scheinost, A. C.; Steudtner, R.; Hübner, R.; Weiss, S.; Bok, F.;

Originally published:

September 2016

Environmental Science & Technology 50(2016)19, 10413-10420

DOI: <https://doi.org/10.1021/acs.est.6b02399>

Perma-Link to Publication Repository of HZDR:

<https://www.hzdr.de/publications/Publ-23676>

Release of the secondary publication
on the basis of the German Copyright Law § 38 Section 4.

1 **Neptunium^V retention by siderite under anoxic conditions:**
2 **Formation of nanoparticulate NpO₂ and Np^{IV} pentacarbonate**

3
4 *Andreas C. Scheinost^{*‡,§} Robin Steudtner[‡], René Hübner[†], Stephan Weiss[‡]*

5
6 [‡] Institute of Resource Ecology, Helmholtz-Zentrum Dresden - Rossendorf, D-01314,
7 Germany

8 [†] Institute of Ion Beam Physics and Materials Research, Helmholtz-Zentrum Dresden -
9 Rossendorf, D-01314, Germany

10 [§] The Rossendorf Beamline at ESRF, F-38043 Grenoble, France

11
12 **Abstract.** The Np^V reactions with siderite, an Fe^{II} carbonate mineral with relevance for the
13 near-field of high-level radioactive waste repositories, were investigated under anoxic
14 conditions within the stability field of siderite (pH 7 to 13). Batch sorption experiments show
15 that siderite has a high solid-water distribution coefficient ($\log R_d > 5$) for aqueous Np^VO₂⁺
16 across the investigated pH range. In comparison to the redox-inert carbonate calcite, this
17 $\log R_d$ is three orders of magnitude higher, and comparable to the $\log R_d$ of the tetravalent
18 actinide Th on calcite. Np L₃-edge X-ray absorption near-edge structure (XANES)
19 spectroscopy confirmed that Np associated to siderite was reduced from the pentavalent to
20 the tetravalent oxidation state. The local structure of the Np^{IV} phase, which was probed by
21 extended X-ray absorption fine-structure (EXAFS) spectroscopy indicated the formation of
22 NpO₂-like nanoparticles with diameter < 1 nm, further corroborated by high-resolution
23 transmission electron microscopy (HR-TEM). The low solubility of these NpO₂-like
24 nanoparticles, along with their negligible surface charge at neutral pH conditions which
25 favors particle aggregation, suggest an efficient retention of Np in the near-field of

26 radioactive waste repositories. When Np^{V} was added to ferrous carbonate solution, the
27 subsequent precipitation of siderite did not lead to a structural incorporation of Np^{IV} by
28 siderite, but caused formation of Np^{IV} pentacarbonate, a hitherto enigmatic phase, while the
29 penta-carbonates of U^{IV} and Pu^{IV} have been identified before.

30

31 **Introduction**

32 Nuclear power generation has left behind a legacy of high-level radioactive waste, which
33 needs to be kept safe for hundreds of thousands of years. The disposal of this waste in deep
34 geological formations behind multiple barriers is a concept favored by many power
35 producing countries to ensure a lasting protection of people and the environment. The
36 multiple barrier system consists of three principal parts, an engineered barrier (copper or
37 stainless steel containers), a geo-engineered barrier (clay-based backfill-material, e.g.
38 bentonite) and the geological barrier (argillaceous, granitic or salt host rock).¹ Many of these
39 components contain or form Fe^{II} -bearing minerals, which may act as scavenger for
40 potentially released radionuclides by their reducing power and sorption capacity. Steel
41 containers are likely to corrode under near-field conditions, forming for instance magnetite,
42 siderite, chukanovite and Fe-phyllsilicates in contact with clay backfill,^{2, 3} magnetite and
43 hydrous Fe^{II} oxides in contact with brine,⁴ and Fe^{II} sulfides in the presence of sulfate
44 reducing bacteria.⁵ Such Fe^{II} -bearing minerals occur also naturally in clay rocks; e.g. MX80
45 bentonite considered as backfill material contains 0.7 % siderite and 0.3% pyrite, and
46 Opalinus clay considered as host rock in Switzerland contains 6% siderite and 0.9% pyrite.^{6,}

47 ⁷

48 Spent nuclear fuel consists mainly of the original uranium dioxide (~95%) and its fission
49 products (lanthanides, technetium, selenium, noble gases and cesium, ~4%). Neutron

50 absorption and decay reactions lead to the formation of plutonium isotopes (~1%) and the
51 minor actinides neptunium, americium and curium (<0.1% of typical burnt fuel). The redox-
52 sensitive elements uranium, plutonium, technetium, selenium have been shown to be
53 efficiently immobilized by sorption and redox reactions on Fe^{II}-bearing minerals ^{4, 8-14} Much
54 less work has been conducted on the redox-driven (anoxic) immobilization of the minor
55 actinide neptunium, although its major radionuclide ²³⁷Np has a very long half life (2.14 Mio
56 years) and contributes significantly to the long-term radiotoxicity of spent fuel. Work
57 attempting to elucidate the mechanisms of Np reduction by mineral surfaces is even more
58 scarce. Np^V was found to be much more strongly retained by magnetite under anoxic
59 conditions than under normal atmosphere; using a liquid extraction technique, Np associated
60 with the solid phase was determined to be tetravalent. ¹⁵ In comparison to aqueous Fe^{II}, the
61 reduction by magnetite was 3 orders of magnitude faster. ¹⁶ A pioneering study employing
62 EXAFS spectroscopy showed that Np^V was only weakly taken up by mackinawite, forming
63 rather surprisingly a mononuclear Np^{IV} sorption complex coordinated to both O and S. ¹⁷ In
64 the presence of green rust, Np^V was rapidly sorbed and reduced to Np^{IV} at the edges of the
65 hexagonal platelets; the authors suggest formation of Np^{IV} particles, but their identification
66 by TEM remained elusive. ¹⁸ Np^V reacted with Opalinus clay was reduced to Np^{IV} and
67 showed a strong association with pyrite particles embedded in the clay matrix; the exact
68 nature of the reduced Np^{IV} could not be identified, but the authors excluded formation of
69 NpO₂ due to the absence of Np-Np backscattering contributions in Np L₃-edge EXAFS
70 spectra. ¹⁹ Biotite and chlorite with structural Fe^{II} fully reduced Np^V to Np^{IV}, and
71 nanoparticulate NpO₂ formed as identified by EXAFS. ²⁰ In the presence of Ti-doped
72 magnetite, sorption of Np^V was high at pH values 5 and 7, while the sorption at pH 3 was
73 low, but increased with Ti-doping most likely because of the increasing Fe^{II} fraction to
74 counterbalance the charge of structural Ti^{IV}. Using Np L₃-edge XANES and EXAFS, the

75 reaction product could be identified as a Np^{IV} species, while the absence of Np-Np
76 backscattering contradicted formation of NpO_2 .²¹ The authors claim formation of an
77 innersphere sorption complex, but fitted Np-Fe and Np-Ti coordination numbers between 5
78 and 7 would rather suggest structural incorporation by magnetite or a secondary Fe phase. In
79 conclusion, the few studies on Np uptake by Fe^{II} -bearing minerals under anoxic conditions
80 show sorption and reduction to Np^{IV} , but the reaction mechanism and the end product, i.e.
81 sorption complexation vs. structural incorporation vs. NpO_2 precipitation, often remain
82 elusive.

83 The objective of our study was therefore, to investigate the Np reduction products under
84 strictly anoxic atmosphere by a combination of Np L_3 -edge XAFS spectroscopy and electron
85 microscopy. As Fe^{II} -bearing mineral phase, the Fe^{II} carbonate siderite was selected because
86 of its relevance for many high-level radioactive waste scenarios as outlined above. The extent
87 of reduction as well as the reduction kinetics of siderite (or the hydroxocarbonate
88 chukanovite) are smaller than that of other Fe^{II} -bearing minerals, most likely because of a
89 larger bandgap preventing a free electron flow from the structure, and also because dissolved
90 carbonate might form complexes with Fe^{II} and the oxidant, thereby potentially competing
91 with the Fe-oxidant redox reaction. Nevertheless, siderite reduced Se^{IV} to elemental selenium,
92 and Pu^{V} to $\text{Pu}^{\text{IV}}\text{O}_2$ -like solids, hence we expected that Np^{V} would also be reduced by siderite.

93 11, 22

94

95 **Materials and Methods**

96 **Caution!** ²³⁷Np is a radioactive isotope and an α -emitter. It should be handled in dedicated
97 facilities with appropriate equipment for radioactive materials to avoid health risks caused
98 by radiation exposure.

99 Generally, all sample manipulations, including mineral synthesis and washing, UV-vis
100 measurements, and preparation of samples for XAS measurements, were carried out under
101 anoxic conditions in a nitrogen glove-box with 0 – 5 ppmv O₂. Experiments were carried out
102 at RT (23 ± 3°C); deionized (18.2 MΩ cm Milli-Q), degassed (O₂ and CO₂ free) water was
103 used for all purposes.

104 **Siderite synthesis and characterization.** A siderite (Fe^{II}CO₃) suspension ([Fe_{tot}] = 0.2 M)
105 was prepared by slowly mixing 100 mL of a 0.4 M Fe^{II}Cl₂ solution with 100 mL of a 0.8 M
106 Na₂CO₃ solution²³. The light gray precipitate was washed with 0.1 M NaCl (at least 3
107 washing cycles) and kept in suspension in 0.1 M NaCl. Siderite is extremely oxidation-
108 sensitive and not stable in suspension with an ionic strength lower than 0.1 M, as indicated by
109 the rapid appearance of brownish Fe^{III} oxyhydroxides like goethite.^{24, 25} Raman spectroscopic
110 measurements were carried out with a Raman-microscope (HORIBA Jobin Yvon LabRAM
111 Aramis Vis) using an Argon-Laser (437 nm) with an output energy of 0.2 mW as light source
112 and confirmed the phase identity and purity (see Fig. S1 in SI). An isoelectric point at 10.1
113 was determined by zeta potential measurements using a Laser-Doppler-Electrophoresis
114 instrument (Zetasizer nano-ZS, Malvern Instruments Ltd.) (Fig. S2).

115 **Np(V) stock solution.** A 0.056 M Np^V stock solution in 1.0 M HClO₄ was prepared from
116 neptunium (²³⁷Np) dioxide (CEA-Marcoule, France), according to a previously reported
117 procedure²⁶. The pentavalent oxidation state of Np was prepared by electrochemical
118 reduction from Np^{VI} and verified by UV-VIS-NIR spectroscopy. This solution was diluted
119 with degassed deionized water to obtain a stock solution of 10⁻³ M Np^V.

120 **Batch sorption.** The Np^V retention by Fe^{II}CO₃ was investigated in the pH range 7 to 13 by
121 batch experiments. For pre-equilibration, Fe^{II}CO₃ suspensions (S/L ratio of 1 g/L) were
122 prepared in 0.1 M NaCl background electrolyte and continuously shaken on a horizontal

123 shaker for 48 h, with pH values initially adjusted and readjusted if necessary. Then, aliquots
124 of the Np^{V} stock solution were added to the $\text{Fe}^{\text{II}}\text{CO}_3$ suspensions to obtain the final Np^{V}
125 concentration of $2 \cdot 10^{-5}$ M. The pH values were readjusted immediately. For sorption, the
126 samples were shaken on a horizontal shaker up to 3 weeks, whereby the pH was monitored
127 and readjusted if necessary. Finally, the remaining suspensions were centrifuged for phase
128 separation (60 min, $3200\times g$). The final Np concentration in the supernatant was determined
129 by liquid scintillation counting (LSC, Winspectral α/β , Wallac 1414, Perkin Elmer) using α/β
130 discrimination with a lower detection limit of $\leq 10^{-9}$ M. The distribution coefficient R_d in L/kg
131 was calculated with

$$132 \quad R_d = \frac{c_{ini} - c_{eq}}{c_{eq}} \cdot \frac{V}{m},$$

133 where c_{ini} and c_{eq} (mol/L) are the initial and equilibrium Np concentration in solution, V (L)
134 the sample volume and m (kg) the mass of siderite.

135 **Np siderite coprecipitation.** In addition to the batch sorption experiments, where Np^{V} was
136 added to pre-synthesized siderite, we also conducted a Np^{V} -siderite coprecipitation
137 experiment to study the eventual structural incorporation of Np. This experiment was
138 performed like the pure mineral synthesis described before, except that an appropriate aliquot
139 of the Np stock solution to obtain a nominal loading Np/siderite of 4705 mg/kg was slowly
140 added to the $\text{Fe}^{\text{II}}\text{Cl}_2$ solution, before adding the Na_2CO_3 solution to initiate the siderite
141 precipitation.

142 **X-ray absorption spectroscopy.** We selected a sorption time series at $\text{pH } 7.7 \pm 0.3$, i.e. in the
143 pH range of the lowest siderite solubility,²⁷ at ionic strength of 0.1 M and after reaction times
144 of 1 h, 1 d, 7 d and 21 d, two additional sorption samples at the same pH, a reaction time of 7
145 d, and an ionic strength of 0.001 and 1 M, and the coprecipitation sample (Table S1). After

146 phase separation by centrifugation, the solids were filled into double-confinement, heat-
147 sealed polyethylene sample holders inside the anoxic glovebox. The samples were then
148 removed from the glovebox and immediately flash-frozen in LN₂ and stored in an LN₂ dewar
149 to prevent oxygen diffusion into the samples and to freeze-in chemical reactions until XAS
150 measurements. After transport to the Rossendorf Beamline at ESRF (Grenoble, France), the
151 samples were individually removed from the LN₂ dewar and transferred to a closed-cycle He
152 cryostat operating at 10 K within less than 30 sec for XAS measurements. XAS (XANES and
153 EXAFS) measurements were carried out in fluorescence mode at the Np- L_{III} edge (17610
154 eV) using a 13-element high-purity Ge solid state detector (Canberra) with digital signal
155 analysis (XIA XMap). The polychromatic synchrotron beam was monochromatized using a
156 pair of water-cooled Si(111) crystals, and higher-order harmonics were rejected by a Rh-
157 coated 1.3-m long collimating mirror before the double-crystal monochromator, and a 1.2-m
158 long Rh-coated toroidal mirror after the monochromator. Between 6 and 12 individual XAS
159 scans were energy-calibrated against a simultaneously measured Y foil (17038 eV), corrected
160 for fluorescence deadtime and averaged using the SIXpack,²⁸ while subsequent data
161 reduction steps and shell fits were conducted using WinXAS.²⁹ Theoretical backscattering
162 paths were calculated with FEFF8.2 using crystal structures of NpO₂ and siderite (with one
163 Fe replaced by Np).³⁰⁻³² Reference spectra for the Np^{IV} aquo complex³³ and for NpO₂³⁴ were
164 downloaded from AcReDaS, the online actinide reference database for spectroscopy.³⁵

165 **Transmission electron microscopy (TEM).** A sample ($[\text{Np}^{\text{V}}]_{\text{ini}} = 2 \cdot 10^{-5} \text{ M}$, $s/l = 0.1 \text{ g} \cdot \text{L}^{-1}$,
166 $I = 0.1 \text{ M}$ (NaCl), reacted for 7 d under anoxic conditions) was prepared by disposing a drop
167 of the Np-siderite suspension on a carbon-coated copper grid (400 mesh, S 160, Plano
168 GmbH) and drying it under an inert gas atmosphere. Bright-field TEM and high-resolution
169 TEM (HRTEM) images were collected on an image C_s-corrected Titan 80-300 electron
170 microscope (FEI) operated at 300 kV. Selected area electron diffraction (SAED) patterns

171 were acquired from a specimen area of 190 nm in diameter. Energy-dispersive X-ray
172 spectroscopy (EDXS) was performed in scanning TEM mode with a Li-drifted silicon
173 detector (EDAX).

174

175 **Results and discussion**

176 The Np^{V} uptake by siderite is very high with $\log R_{\text{d}}$ values always above 5 and little variation
177 across the pH range 7 to 13 (Fig. 1 top)). In comparison to the Np^{V} uptake by the (redox-
178 inactive) carbonate calcite, these $\log R_{\text{d}}$ values are three orders of magnitude higher,³⁶ and
179 much more similar to values obtained for the tetravalent actinide, Th, on calcite,³⁷ in both
180 cases at comparable pH. Hence the high $\log R_{\text{d}}$ values are a first indication that Np^{V} was
181 indeed reduced to Np^{IV} by siderite. Further support comes from by the thermodynamic
182 calculation, showing that at the measured Eh values at pH 8, 10 and 12, the equilibrium
183 should be dominated by NpO_2 (Fig. 1 bottom).

184 Figure 2 shows the Np-L_{III} edge XANES spectra of the siderite sorption time series at pH 7.7
185 ± 0.3 , and of the coprecipitation sample. All spectra are well aligned and correspond both in
186 edge and white-line position with the two Np^{IV} references, NpO_2 and an Np^{IV} aquo complex.
187^{33, 34} This is further confirmed by the XANES edge energies as determined by the knot of the
188 second derivative, which vary by less than 0.3 eV from the average of 17613.5 eV (Table 1).
189 Therefore, Np^{V} is fully reduced to Np^{IV} in all systems, even already after the shortest sorption
190 time of 1 h, and also in the coprecipitation sample.

191

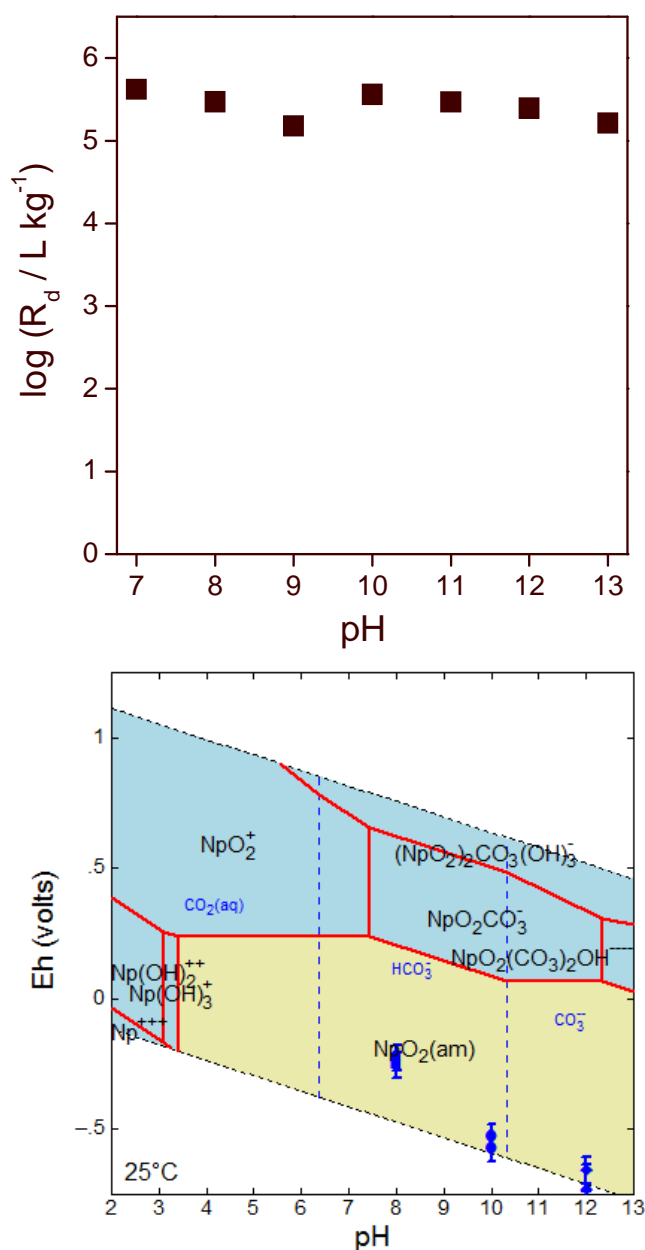


Figure 1. Top: Np solid/liquid distribution coefficient in the siderite system as function of pH. $[\text{Np}^{\text{V}}]_{\text{initial}} = 2 \cdot 10^{-5} \text{ M}$, $s/l = 1 \text{ g} \cdot \text{L}^{-1}$, $I = 0.1 \text{ M NaCl}$, after 1 week reaction time under anoxic N_2 . Bottom: Eh-pH diagram calculated for the chemical system $2 \cdot 10^{-5} \text{ M Np}^{\text{V}}$ in 0.1 M NaCl solution in presence of siderite under anoxic conditions at 25°C . Thermodynamic data of the Lawrence Livermore National Laboratory thermo database were supplemented by the most recent NEA database.^{38, 39} Experimental results represented by blue symbols for the batch experiments.

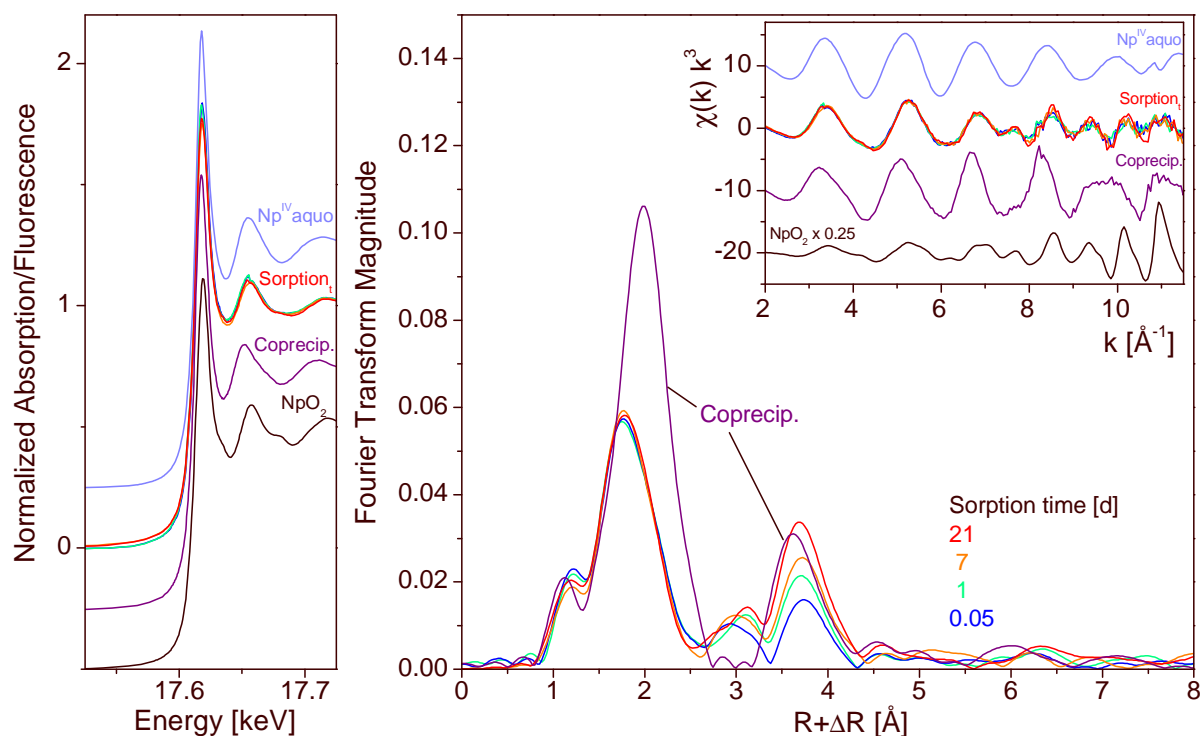


Figure 2. Neptunium L_{III} -edge XAS spectra of selected siderite sorption and coprecipitation samples ($\text{pH } 7.7 \pm 0.3$) along with Np references. Left: XANES spectra, right: EXAFS Fourier transform magnitude and corresponding $\chi(k)$ spectra as insert.

192 The EXAFS Fourier transform magnitudes of the sorption samples show a coordination shell
 193 at $R+\Delta R=1.8 \text{ \AA}$ (uncorrected for phase shift), which is fitted by about 8 oxygen atoms at a
 194 distance of $2.34 - 2.35 \text{ \AA}$. Note that the small peak at the left side of this coordination shell
 195 cannot be fitted with a Np-O distance of 1.87 \AA as would be expected for the $-\text{yl}$ group of
 196 Np^{V} ; they constitute instead a truncation artifact of the Fourier transformation arising from
 197 the relatively short k -range. A second peak at $R+\Delta R=3.7 \text{ \AA}$ increases in height with sorption
 198 time. Wavelet analysis of this peak reveals an amplitude maximum at $k>10 \text{ \AA}^{-1}$, in line with
 199 backscattering by a heavy element.⁴⁰ Correspondingly, this shell could be fitted with Np
 200 atoms at a distance of $3.82 - 3.84 \text{ \AA}$.

201

Table 1. Np-L_{III} XANES edge energies and EXAFS fit results of Np siderite samples and references ($S_0^2=0.9$, fit range 2.0 – 11.5 Å⁻¹).

Sample	E_0 [eV]	First shell			Second shell			ΔE_0 [eV]	χ^2_{res} %
		CN ¹	R ² [Å ²]	σ^2 ³ [Å]	CN	R [Å]	σ [Å ²]		
Sorption 1 h (0.1 M)	17613.3	8.0 O	2.35	0.0100	2.1 Np	3.83	0.0026	7.1	19.3
Sorption 1 d (0.1 M)	17613.4	7.7 O	2.35	0.0100	4.4 Np	3.84	0.0100	7.6	19.8
Sorption 7 d (0.1 M)	17613.3	7.8 O	2.34	0.0100	3.9 Np	3.83	0.0054	7.4	16.4
Sorption 21 d (0.1 M)	17613.5	7.9 O	2.34	0.0100	3.8 Np	3.82	0.0034	7.0	13.8
Sorption 0.001 M (7 d)	17613.6	8.4 O	2.35	0.0100	3.4 Np	3.83	0.0027	7.4	14.6
Sorption 1 M (7 d)	17613.6	8.0 O	2.34	0.0100	3.6 Np	3.83	0.0060	7.3	15.5
Sid-coprecipitate	17613.8	9.6 O	2.41	0.0048	4.2 4.2 ^c 8.4 ^{2c} 4.2 ^c C _{bid} -O _{dist} -C _{bid}	C _{bid} 2.87 O _{dist} 4.14 ^c C _{bid} -O _{dist} 4.14 ^c C _{bid} -O _{dist} -C _{bid} 4.14 ^c	0.0010 0.0016 ^c 0.0016 ^c 0.0016 ^c	14.6	12.8
Np ^{IV} aquo	17613.8	11.6 O	2.39	0.0083				9.4	5.2
NpO ₂	17613.6	8 O	2.35	0.0043	12 24 O	Np 3.85 4.48	0.0010 0.0010	9.6	19.4
NpO ₂ crystal structure ⁴¹		8 O	2.35		12 24 O	Np 3.84 4.51			

¹ CN: coordination number, error ± 25 %

² R: Radial distance, error ± 0.01 Å

³ σ^2 : Debye-Waller factor, error ± 0.0005 Å²

202 The interatomic distances (R) for these nearest Np–O and Np–Np shells are close to those of
 203 NpO₂. While the coordination numbers (CN) for the Np–O shell are close to 8 as in the cubic
 204 NpO₂ structure, the CNs of the Np–Np path are much lower with larger Debye–Waller factors

205 (σ^2) as compared with those for NpO_2 .⁴¹ A NpO_2 cluster with 1 nm diameter contains 13 Np
206 atoms with an average Np-Np coordination number of 5.5 ($12 \times 5 + 1 \times 12$). This coordination
207 number is significantly higher than the ones derived from EXAFS shell fit (3.5 per average
208 for all sorption samples), suggesting an even smaller average particle size, or cation
209 vacancies. Similar trends were observed for nanocrystalline Np dioxide particles formed after
210 dilution of aqueous Np^{IV} carbonate complexes³⁴ and for other An^{IV} oxide/hydroxide species.
211⁴²⁻⁴⁴ Therefore, the EXAFS analysis suggests that Np^{V} reduction at the siderite surface leads
212 to the formation of either small particles of crystalline NpO_2 or to structurally disordered
213 Np^{IV} oxide/hydroxide. While the peak height of the Np-Np shell increases with increasing
214 sorption time, suggesting the growth of nanoparticles with time, the shell fit data suggest a
215 more complicated process: between 1 h and 1 d sorption time, the CN doubles from 2 to 4,
216 but then remains constant. At the same time, the Debye-Waller factor increases from 0.0026
217 to 0.0100 \AA^2 , and decreases thereafter with increasing sorption time to 0.0034 \AA^2 . This
218 suggests that the initial particles are small, but well ordered, and then grow with high
219 disorder, which subsequently obtain a higher degree of order with sorption time. Ionic
220 strength of the background electrolyte also shows a significant effect on the Debye-Waller
221 factor, which increases from 0.0027 to 0.0054 to 0.0060 \AA^2 , when the ionic strength increases
222 from 0.001 to 0.1 to 1 M for a constant reaction time of 7 d. Therefore, increasing
223 background electrolyte concentrations seem to increasingly interfere with the crystallization
224 process.

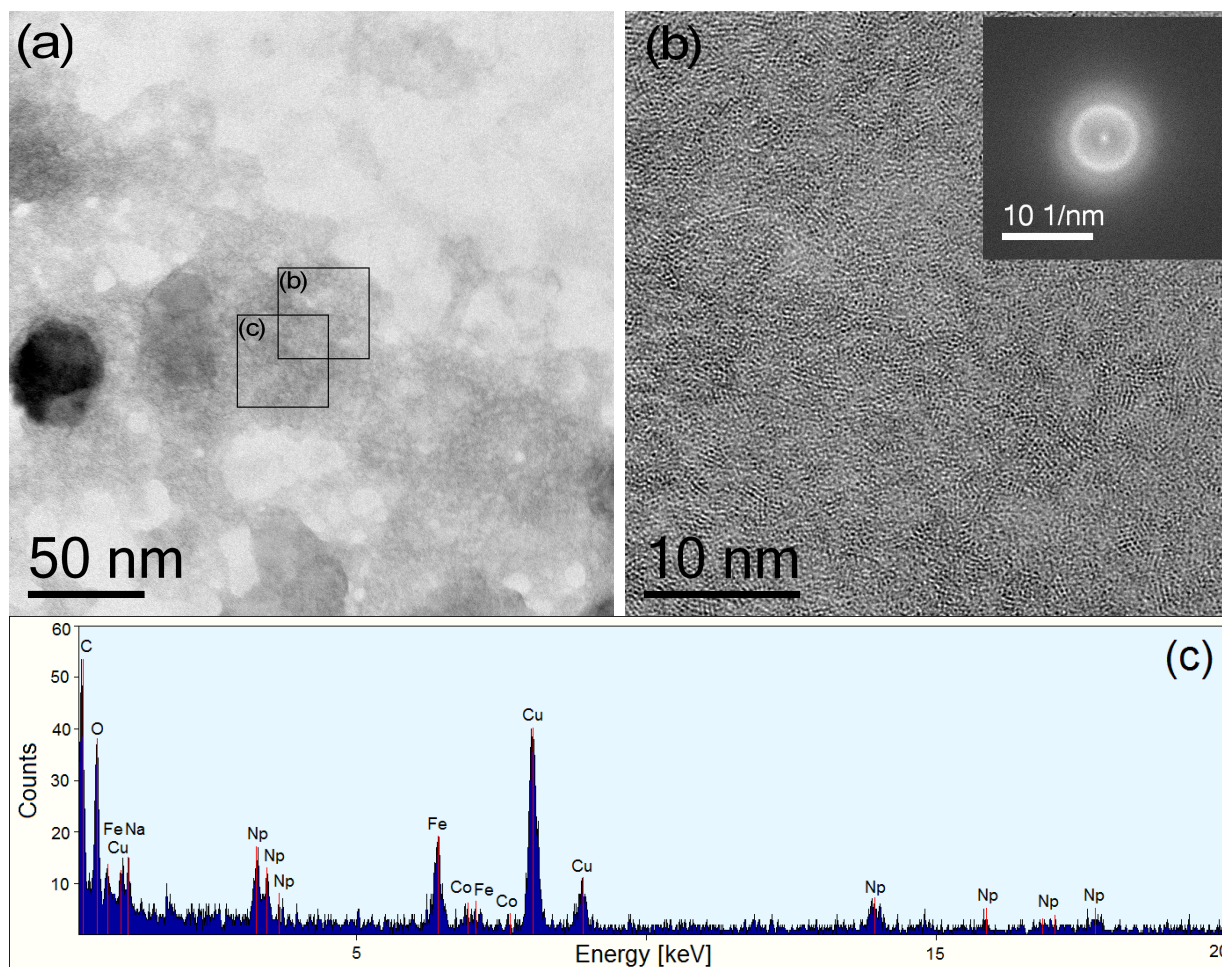


Figure 3. (a) Bright-field TEM micrograph of a dried Np siderite suspension ($[\text{Np}^{\text{V}}]_{\text{ini}} = 2 \cdot 10^{-5} \text{ M}$, $s/l = 0.1 \text{ g} \cdot \text{L}^{-1}$, $\text{pH}=7.6$, $I = 0.1 \text{ M}$ (NaCl), after 7 d under anoxic conditions). (b) HR-TEM image of area (b). (c) Energy-dispersive X-ray (EDX) spectrum obtained in scanning TEM mode from the area (c).

225 To further characterize its microstructure, a dried Np siderite suspension was analyzed using
 226 TEM. A corresponding bright-field TEM micrograph is shown in Fig. 3a. While the black
 227 particle with a diameter of approximately 40 nm is siderite, the gray areas arise from particles
 228 much smaller than siderite. According to the HRTEM image shown in Fig. 3b, their average
 229 size is in the order of $\leq 1 \text{ nm}$. Corresponding to this small particle size, the Fourier transform
 230 in the inset does not show sharp distinctive rings. The dominant presence of Np and O
 231 determined in an adjacent region by energy-dispersive X-ray (EDX) spectroscopy (Fig. 3c)
 232 confirms that these small particles constitute indeed the Np phase (Note that C and Cu stem

233 from the TEM support grid, and Fe and Co from the objective lens pole piece; however, a
234 contribution of siderite to the Fe fluorescence line cannot be excluded). Extended electron
235 irradiation (1-2 min.) induced particle growth, and selected area electron diffraction of those
236 irradiated regions led to diffraction patterns with distinctive diffraction rings which are in
237 agreement with the fluorite-type NpO_2 structure ($Fm\bar{3}m$) (not shown here).⁴⁵ Thus, the TEM
238 investigations support the EXAFS analysis that Np^{IV} is precipitated as precursor of
239 nanoparticulate NpO_2 with particle sizes below 1 nm.

240 In contrast to the sorption samples, the EXAFS Fourier transform magnitude of the
241 coprecipitation sample shows a much higher and more distant coordination shell (Fig. 2
242 right), which could be fitted with ~ 10 oxygen atoms at a distance of 2.41 Å, i.e. not
243 commensurate to the cubic NpO_2 structure (Table 1). Furthermore, the second shell is at a
244 shorter distance than the Np-Np shell of NpO_2 . Wavelet analysis of this shell shows a
245 maximum of k at about 8 \AA^{-1} , hence discards that this peak arises from Np-Np backscattering.
246 The spectrum is in fact similar to compounds where carbon is bidentately coordinated, like in
247 Ce^{IV} or U^{IV} carbonate compounds.⁴⁶ This was confirmed by a shell fit based on this bidentate
248 arrangement, which gives rise to very characteristic multiple scattering paths involving the
249 nearest C_{bid} and the next nearest, distal O (O_{dist}) atom of the carbonate molecule. The Np-O
250 coordination number of ~ 10 as well as the Np- C_{bid} coordination number of 4.2 (theoretically
251 5) confirm the formation of $\text{Np}^{\text{IV}}(\text{CO}_3)_5$ units very similar to those found for U^{IV} and Pu^{IV}
252 before, and in line with the similar complex formation constants of all three actinides.⁴⁶⁻⁴⁸ As
253 expected for the slightly smaller ionic radius of Np^{IV} versus U^{IV} , the fitted distances are about
254 0.02 Å shorter than for the U^{IV} carbonate unit (Table 1). Analogous to U^{IV} , the Np^{IV}
255 pentacarbonate unit may exist either as aquo-anion complex,³⁴ or in the solid state with e.g.
256 Na for charge compensation and crystal water.⁴⁶ The relatively strong association of this

257 Np^{IV} species with the solid phase (logR_d=4.0) leaves little doubt about the solid-state nature
258 of this Np^{IV} carbonate species, since the potentially 6-fold negative charge of the aquo-anion
259 would prevent strong sorption to the siderite surface. Furthermore, a fit of the spectrum
260 assuming that Np^{IV} resides in the octahedrally coordinated position of Fe^{II} in siderite failed
261 due to the fact that no Np-C shell at a distance of 3.0 to 3.4 Å could be fitted, which would be
262 characteristic for the monodentate coordination of carbon and the cations in siderite.
263 Therefore, our results demonstrate that Np^{IV} does not form part of the siderite structure
264 through co-precipitation, but is entrapped by formation of a Np^{IV} carbonate precipitate.
265 Evidently, the strong complexation of Np with dissolved carbonate prevented the
266 incorporation by siderite. ⁴⁸

267

268

269 **Environmental implications**

270 After reaction of Np^V with siderite, we could demonstrate for the first time the formation of
271 NpO₂-like nanoparticles, while formation of (a significant amount of) monomeric Np^{IV}
272 sorption complexes could be excluded. The formation of a NpO₂-like phase by a surface-
273 mediated redox reaction is in line with results by a recent study showing Np^V reduction by
274 biotite and chlorite with reduced structural iron. ²⁰ It is also in line with formation of UO₂-
275 like nanoparticles upon U^{VI} sorption to e.g. magnetite and mackinawite. ^{49, 50} Interestingly,
276 the strong affinity of Np^{IV} towards carbonate did not prevent the precipitation of the NpO₂-
277 like phase, likewise to the formation of PuO₂ after reaction of Pu^V with the Fe^{II}
278 hydroxocarbonate chukanovite. ¹¹ This can be explained by the relatively low siderite
279 solubility in the investigated pH range. Only when Np^V was added to the 0.8 M carbonate
280 solution prior to siderite precipitation, strong carbonate complexation and subsequent

281 precipitation of a Np^{IV} pentacarbonate took place. Since such high carbonate concentrations
282 are not to be expected under radioactive waste conditions, formation of NpO_2 -like
283 nanoparticles is certainly more relevant for the safety case.

284 The observed high retention of Np by siderite across a relatively wide pH range is
285 encouraging. However, the potential mobilization of the formed NpO_2 -like nanoparticles as
286 colloids may significantly raise the risk of Np migration away from the waste disposal site.^{51,}

287 ⁵² The two-electron transition from U^{VI} to U^{IV} requires the formation of a chemical bond with
288 an electron-providing surface, while the formation of aqueous Fe-U ion pairs can provide
289 only one electron, which kinetically hinders the redox reaction.⁵³ Not surprisingly, TEM

290 images of surface-catalyzed UO_2 show an intimate spatial association with the mineral
291 surface.^{49, 50} This is not the case for the NpO_2 particles, which are diffusely distributed

292 between the siderite particles (Fig. 3 a), thereby suggesting that the single electron required
293 for the Np^{V} reduction might be provided by dissolved Fe^{II} species. This is further supported
294 by the high isoelectric point of siderite (pH 10.1), leading to charge repulsion between the

295 (net) positively charged surface and the cationic $\text{Np}^{\text{V}}\text{O}_2^+$ species prevailing below pH 10,
296 which should also favor a redox reaction between dissolved Np^{V} and Fe^{II} species. Therefore,
297 the NpO_2 -like nanoparticles formed in presence of siderite may have a significant tendency

298 to become detached from the mineral assembly. This does not necessarily mean that they also
299 have a strong tendency to form mobile colloids, since their surface charge is low at
300 circumneutral conditions, which favors their coagulation and causes a relatively fast settling.

301 ³⁴ This, however, may change in the presence of dissolved silica, since then amorphous NpO_2
302 silica structures can form, whose negatively-charged silanol surface groups may provide
303 rather stable colloidal suspensions.⁵⁴

304

305 **Author information**

306 Corresponding Author

307 *Phone: ++33 476 88 2462. E-mail: scheinost@esrf.fr

308

309 **Notes**

310 The authors declare no competing financial interest.

311 **Acknowledgments**

312 This work funded by BMWi (02NUK019D, IMMORAD). We thank the ROBL team, and
313 Maria Berger, Anika Maffert, Christa Müller, Ina Kappler and Sophia Kostudis for their
314 invaluable help. Support by the Ion Beam Center (IBC) at HZDR is gratefully acknowledged.
315 Paul Wersin (University of Berne) has performed the thermodynamic calculations given in
316 SI.

317

318 **References**

- 319 (1) Sellin, P.; Leupin, O. X. The use of clay as an engineered barrier in radioactive waste management - A
320 review. *Clays and Clay Minerals* **2013**, *61* (6), 477-498.
- 321 (2) Schlegel, M. L.; Bataillon, C.; Blanc, C.; Pret, D.; Foy, E. Anodic activation of iron corrosion in clay
322 media under water-saturated conditions at 90 degrees C: Characterization of the corrosion interface.
323 *Environmental Science & Technology* **2010**, *44* (4), 1503-1508.
- 324 (3) Wersin, P.; Jenni, A.; Mader, U. K. Interaction of corroding iron with bentonite in the ABM1
325 experiment at Aspö, Sweden: A microscopic approach. *Clays and Clay Minerals* **2015**, *63* (1-2), 51-68.
- 326 (4) Grambow, B.; Smailos, E.; Geckeis, H.; Müller, R.; Hentschel, H. Sorption and reduction of uranium(VI)
327 on iron corrosion products under reducing saline conditions. *Radiochimica Acta* **1996**, *74*, 149-154.
- 328 (5) El Hajj, H.; Abdelouas, A.; El Mendili, Y.; Karakurt, G.; Grambow, B.; Martin, C. Corrosion of carbon
329 steel under sequential aerobic-anaerobic environmental conditions. *Corrosion Science* **2013**, *76*, 432-440.
- 330 (6) Marques Fernandes, M.; Ver, N.; Baeyens, B. Predicting the uptake of Cs, Co, Ni, Eu, Th and U on
331 argillaceous rocks using sorption models for illite. *Applied Geochemistry* **2015**, *59*, 189-199.
- 332 (7) Karnland, O. *Chemical and mineralogical characterization of the bentonite buffer for the acceptance*
333 *control procedure in a KBS-3 repository*; Technical Report SKB TR-10-60: 2010.
- 334 (8) Myneni, S. C. B.; Tokunaga, T. K.; Brown, G. E. Abiotic selenium redox transformations in the presence
335 of Fe(II,III) oxides. *Science* **1997**, *278*, 1106-1109.
- 336 (9) Scheinost, A. C.; Charlet, L. Selenite reduction by mackinawite, magnetite and siderite: XAS
337 characterization of nanosized redox products. *Environ. Sci. Technol.* **2008**, *42* (6), 1984-1989.
- 338 (10) Jaisi, D. P.; Dong, H.; Plymale, A. E.; Fredrickson, J. K.; Zachara, J. M.; Heald, S.; Liu, C. Reduction and
339 long-term immobilization of technetium by Fe(II) associated with clay mineral nontronite. *Chemical Geology*
340 **2009**, *264* (1-4), 127-138.
- 341 (11) Kirsch, R.; Fellhauer, D.; Altmaier, M.; Neck, V.; Rossberg, A.; Fanghänel, T.; Charlet, L.; Scheinost, A. C.
342 Oxidation state and local structure of plutonium reacted with magnetite, mackinawite and chukanovite.
343 *Environ. Sci. Technol.* **2011**, *45* (17), 7267-7274.

- 344 (12) Um, W.; Chang, H.-S.; Icenhower, J. P.; Lukens, W. W.; Serne, R. J.; Qafoku, N. P.; Westsik, J. H., Jr.;
345 Buck, E. C.; Smith, S. C. Immobilization of 99-Techneium (VII) by Fe(II)-Goethite and Limited Reoxidation.
346 *Environmental Science & Technology* **2011**, *45* (11), 4904-4913.
- 347 (13) Huber, F.; Schild, D.; Vitova, T.; Rothe, J.; Kirsch, R.; Schafer, T. U(VI) removal kinetics in presence of
348 synthetic magnetite nanoparticles. *Geochim. Cosmochim. Ac.* **2012**, *96*, 154-173.
- 349 (14) Peretyazhko, T. S.; Zachara, J. M.; Kukkadapu, R. K.; Heald, S. M.; Kutnyakov, I. V.; Resch, C. T.; Arey, B.
350 W.; Wang, C. M.; Kovarik, L.; Phillips, J. L.; Moore, D. A. Pertechneate (TcO₄⁻) reduction by reactive ferrous
351 iron forms in naturally anoxic, redox transition zone sediments from the Hanford Site, USA. *Geochimica Et*
352 *Cosmochimica Acta* **2012**, *92*, 48-66.
- 353 (15) Nakata, K.; Nagasaki, S.; Tanaka, S.; Sakamoto, Y.; Tanaka, T.; Ogawa, H. Sorption and reduction of
354 neptunium(V) on the surface of iron oxides. *Radiochimica Acta* **2002**, *90* (9-11), 665-669.
- 355 (16) Nakata, K.; Nagasaki, S.; Tanaka, S.; Sakamoto, Y.; Tanaka, T.; Ogawa, H. Reduction rate of
356 neptunium(V) in heterogeneous solution with magnetite. *Radiochimica Acta* **2004**, *92* (3), 145-149.
- 357 (17) Moyes, L. N.; Jones, M. J.; Reed, W. A.; Livens, F. R.; Charnock, J. M.; Mosselmans, J. F. W.; Hennig, C.;
358 Vaughan, D. J.; Patrick, R. A. D. An X-ray absorption spectroscopy study of neptunium(V) reactions with
359 mackinawite (FeS). *Environ. Sci. Technol.* **2002**, *36* (2), 179-183.
- 360 (18) Christiansen, B. C.; Geckeis, H.; Marquardt, C. M.; Bauer, A.; Roemer, J.; Wiss, T.; Schild, D.; Stipp, S. L.
361 S. Neptunyl (NpO₂⁺) interaction with green rust, GR(Na,SO₄). *Geochimica Et Cosmochimica Acta* **2011**, *75* (5),
362 1216-1226.
- 363 (19) Frohlich, D. R.; Amayri, S.; Drebert, J.; Grolimund, D.; Huth, J.; Kaplan, U.; Krause, J.; Reich, T.
364 Speciation of Np(V) uptake by Opalinus Clay using synchrotron microbeam techniques. *Anal. Bioanal. Chem.*
365 **2012**, *404* (8), 2151-2162.
- 366 (20) Brookshaw, D. R.; Patrick, R. A. D.; Bots, P.; Law, G. T. W.; Lloyd, J. R.; Mosselmans, J. F. W.; Vaughan,
367 D. J.; Dardenne, K.; Morrie, K. Redox Interactions of Tc(VII), U(VI), and Np(V) with Microbially Reduced Biotite
368 and Chlorite. *Environmental Science & Technology* **2015**, *49* (22), 13139-13148.
- 369 (21) Wylie, E. M.; Olive, D. T.; Powell, B. A. Effects of Titanium Doping in Titanomagnetite on Neptunium
370 Sorption and Speciation. *Environmental Science & Technology* **2016**, *50* (4), 1853-1858.
- 371 (22) Scheinost, A. C.; Kirsch, R.; Banerjee, D.; Fernandez-Martinez, A.; Zaenker, H.; Funke, H.; Charlet, L. X-
372 ray absorption and photoelectron spectroscopy investigation of selenite reduction by FeII-bearing minerals. *J.*
373 *Contam. Hydrol.* **2008**, *102* (3-4), 228-245.
- 374 (23) Charlet, L.; Wersin, P.; Stumm, W. Surface-charge of MnCO₃ and FeCO₃. *Geochim. Cosmochim. Acta*
375 **1990**, *54* (8), 2329-2336.
- 376 (24) Postma, D. Pyrite and siderite oxidation in swamp sediments. *Journal of Soil Science* **1983**, *34* (1), 163-
377 182.
- 378 (25) Scheinost, A. C.; Schwertmann, U. Color identification of iron oxides and hydroxysulfates - Use and
379 limitations. *Soil Science Society of America Journal* **1999**, *63*, 1463-1471.
- 380 (26) Ikeda-Ohno, A.; Hennig, C.; Rossberg, A.; Funke, H.; Scheinost, A. C.; Bernhard, G.; Yaita, T.
381 Electrochemical and complexation behavior of neptunium in aqueous perchlorate and nitrate solutions.
382 *Inorganic Chemistry* **2008**, *47* (18), 8294-8305.
- 383 (27) Bruno, J.; Wersin, P.; Stumm, W. On the influence of carbonate in mineral dissolution. 2. The solubility
384 of FeCO₃(s) at 25-degrees-C and 1 atm total pressure. *Geochimica et Cosmochimica Acta* **1992**, *56* (3), 1149-
385 1155.
- 386 (28) Webb, S. M. SIXpack: a graphical user interface for XAS analysis using IFEFFIT. *Physica Scripta* **2005**,
387 *T115*, 1011-1014.
- 388 (29) Ressler, T. WinXAS: a program for X-ray absorption spectroscopy data analysis under MS-Windows.
389 *Journal of Synchrotron Radiation* **1998**, *5*, 118-122.
- 390 (30) Ankudinov, A. L.; Rehr, J. J. Relativistic calculations of spin-dependent x-ray-absorption spectra.
391 *Physical Review B* **1997**, *56*, 1712-1728.
- 392 (31) Benedict, U.; Dabos, S.; Dufour, C.; Spirlet, J. C.; Pages, M. Neptunium compounds under high
393 pressure. *Journal of the Less-Common Metals* **1986**, *121*, 461-468.
- 394 (32) Effenberger, H.; Mereiter, K.; Zemann, J. Crystal-structure refinements of magnesite, calcite,
395 rhodochrosite, siderite, smithonite, and dolomite, with discussion of some aspects of the stereochemistry of
396 calcite-type minerals. *Zeitschrift fur Kristallographie* **1981**, *156* (3-4), 233-243.
- 397 (33) Hennig, C. Evidence for double-electron excitations in the L₃-edge x-ray absorption spectra of
398 actinides. *Phys. Rev. B* **2007**, *75* (035120), 035120-1 - 035120-7.

399 (34) Husar, R.; Hübner, R.; Hennig, C.; Martin, P. M.; Chollet, M.; Weiss, S.; Stumpf, T.; Zänker, H.; Ikeda-
400 Ohno, A. Intrinsic formation of nanocrystalline neptunium dioxide under neutral aqueous conditions relevant
401 to deep geological repositories. *Chemical Communications* **2015**, 51 (7), 1301-1304.

402 (35) Rossberg, A.; Scheinost, A. C.; Schmeisser, N.; Rothe, J.; Kaden, P.; Schild, D.; Wiss, T.; Daehn, R.
403 AcReDaS, an Actinide Reference Database for XAS, EELS, IR, Raman and NMR Spectroscopy. In
404 <http://www.hzdr.de/acredas>, 2014.

405 (36) Zavarin, M.; Roberts, S. K.; Hakem, N.; Sawvel, A. M.; Kersting, A. B. Eu(III), Sm(III), Np(V), Pu(V), and
406 Pu(IV) sorption to calcite. *Radiochimica Acta* **2005**, 93 (2), 93-102.

407 (37) Tits, J.; Wieland, E.; Bradbury, M. H.; Eckert, P.; Schaible, A. *The Uptake of Eu(III) and Th(IV) by Calcite*
408 *under Hyperalkaline Conditions*. ; PSI Bericht Nr. 02-03: Villigen, Switzerland, 2002.

409 (38) Lemire, R. J.; Fuger, J.; Nitsche, H.; Potter, P.; Rand, M. H.; Rydberg, J.; Spahiu, K.; Sullivan, J. C.;
410 Ullmann, W. J.; Vitorge, P.; Wanner, H. *Chemical Thermodynamics of Neptunium and Plutonium*. Elsevier:
411 Amsterdam, 2001; p 870.

412 (39) Guillaumont, R.; Fanghänel, T.; Fuger, J.; Grenthe, I.; Neck, V.; Palmer, D. A.; Rand, M. H. *Update on*
413 *the chemical thermodynamics of uranium, neptunium, plutonium, americium and technetium. Chemical*
414 *Thermodynamics Vol. 5*. OECD Nuclear Energy Agency: Elsevier, 2003; Vol. Vol. 5, p 960.

415 (40) Funke, H.; Scheinost, A. C.; Chukalina, M. Wavelet analysis of extended X-ray absorption fine structure
416 data. *Physical Review* **2005**, B 71, 094110.

417 (41) Zachariasen, W. H. Crystal chemical studies of the 5f-series of elements: XII. New compounds
418 representing known structure type. *Acta Crystallographica* **1949**, 2, 388-390.

419 (42) Rothe, J.; Denecke, M. A.; Neck, V.; Müller, R.; Kim, J. I. XAFS investigation of the structure of aqueous
420 thorium(IV) species, colloids, and solid thorium(IV) oxide/hydroxide. *Inorg Chem* **2002**, 41 (2), 249-258.

421 (43) Rothe, J.; Walther, C.; Denecke, M. A.; Fanghanel, T. XAFS and LIBD investigation of the formation and
422 structure of colloidal Pu(IV) hydrolysis products. *Inorg. Chem.* **2004**, 43 (15), 4708-4718.

423 (44) Ikeda-Ohno, A.; Hennig, C.; Tsushima, S.; Scheinost, A. C.; Bernhard, G.; Yaita, T. Speciation and
424 structural study of U(IV) and -(VI) in perchloric and nitric acid solutions. *Inorg. Chem.* **2009**, 48 (15), 7201-7210.

425 (45) Taylor, D. Thermal-expansion data. 2. Binary oxide with the fluorite and rutile structures, MO₂, and
426 the antifluorite structure, M₂O. *Transactions and Journal of the British Ceramic Society* **1984**, 83 (2), 32-37.

427 (46) Hennig, C.; Ikeda-Ohno, A.; Emmerling, F.; Kraus, W.; Bernhard, G. Comparative investigation of the
428 solution species [U(CO₃)₅]⁶⁻ and the crystal structure of Na₆[U(CO₃)₅]·12H₂O. *Dalton Trans.* **2010**, 39 (15), 3744-
429 3750.

430 (47) Clark, D. L.; Conradson, S. D.; Keogh, D. W.; Palmer, P. D.; Scott, B. L.; Tait, C. D. Identification of the
431 limiting species in the plutonium(IV) carbonate system. Solid state and solution molecular structure of the
432 Pu(CO₃)₅ (6-) ion. *Inorg Chem* **1998**, 37 (12), 2893-2899.

433 (48) Guillaumont, R.; Fanghänel, T.; Fuger, J.; Grenthe, I.; Neck, V.; Palmer, D. A.; Rand, M. H. *Update on*
434 *the Chemical Thermodynamics of Uranium, Neptunium, Plutonium, Americium and Technetium*. Elsevier:
435 Amsterdam, 2003.

436 (49) Latta, D. E.; Gorski, C. A.; Boyanov, M. I.; O'Loughlin, E. J.; Kemner, K. M.; Scherer, M. M. Influence of
437 Magnetite Stoichiometry on U-VI Reduction. *Environmental Science & Technology* **2012**, 46 (2), 778-786.

438 (50) Veeramani, H.; Scheinost, A. C.; Monsegue, N.; Qafoku, N. P.; Kukkadapu, R.; Newville, M.; Lanzirrotti,
439 A.; Pruden, A.; Murayama, M.; Hochella Jr., M. F. Abiotic reductive immobilization of U(VI) by biogenic
440 mackinawite. *Environ. Sci. Technol.* **2013**, 47, 2361-2369.

441 (51) Walther, C.; Denecke, M. A. Actinide Colloids and Particles of Environmental Concern. *Chemical*
442 *Reviews* **2013**, 113 (2), 995-1015.

443 (52) Kersting, A. B. Plutonium Transport in the Environment. *Inorg Chem* **2013**, 52 (7), 3533-3546.

444 (53) Liger, E.; Charlet, L.; Van Cappellen, P. Surface catalysis of uranium(VI) reduction by iron(II).
445 *Geochimica et Cosmochimica Acta* **1999**, 63 (19/20), 2939-2955.

446 (54) Husar, R.; Weiss, S.; Hennig, C.; Hübner, R.; Ikeda-Ohno, A.; Zänker, H. Formation of
447 neptunium(IV)-silica colloids at near-neutral and slightly alkaline pH. *Environ. Sci. Technol.* **2015**, 49, 665-671.